NANO LETTERS
Letter
Cite This: Nano Lett. 2018, 18, 3377−3383
pubs.acs.org/NanoLett

Phonon-Mediated Colossal Magnetoresistance in Graphene/Black Phosphorus Heterostructures

Yanpeng Liu,[†,‡] Indra Yudhistira,[‡,§] Ming Yang,[∥] Evan Laksono,[‡,§] Yong Zheng Luo,[‡,§] Jianyi Chen,[†,‡] Junpeng Lu,[‡,§] Yuan Ping Feng,[‡,§] Shaffique Adam,[‡,§] and Kian Ping Loh*[,†,‡]

[†]Department of Chemistry, National University of Singapore, 3 Science Drive 3, Singapore 117543

[‡]Centre for Advanced 2D Materials, National University of Singapore, Singapore 117546

[§]Department of Physics, National University of Singapore, Singapore 117542

[∥]Institute of Materials Research and Engineering, Agency for Science, Technology and Research (A*STAR), 2 Fusionopolis Way, Singapore 138634

Supporting Information

ABSTRACT: There is a huge demand for magnetoresistance (MR) sensors with high sensitivity, low energy consumption, and room temperature operation. It is well-known that spatial charge inhomogeneity due to impurities or defects introduces mobility fluctuations in monolayer graphene and gives rise to MR in the presence of an externally applied magnetic field. However, to realize a MR sensor based on this effect is hampered by the difficulty in controlling the spatial distribution of impurities and the weak magnetoresistance effect at the monolayer regime. Here, we fabricate a highly stable monolayer graphene-on-black phosphorus (G/BP) heterostructure device that exhibits a giant MR of 775% at 9 T magnetic field and 300 K, exceeding by far the MR effects from devices made from either monolayer graphene or few-layer BP alone. The positive MR of the G/BP device decreases when the temperature is lowered, indicating a phonon-mediated process in addition to scattering by charge impurities. Moreover, a nonlocal MR of >10 000% is achieved for the G/BP device at room temperature due to an enhanced flavor Hall effect induced by the BP channel. Our results show that electron−phonon coupling between 2D material and a suitable substrate can be exploited to create giant MR effects in Dirac semimetals.

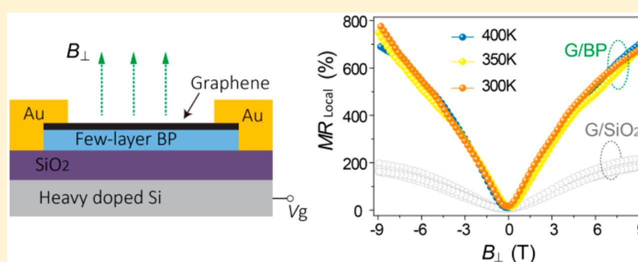

KEYWORDS: *Graphene, black phosphorus, magnetoresistance, phonon-mediated process, nonlocal response*

Magnetic sensing, recording, and memory devices have been revolutionized since the discoveries of giant magnetoresistance (MR) and tunneling magnetoresistance (in metallic spin values or metal/oxide structures).[1,2] The magnitude of MR is an important figure of merit in all of these devices, and there are huge demands for MR sensors that exhibit high sensitivity (large MR response) and low energy consumption, and which are easy to fabricate. Even though the current 3D material-based sensors have relatively high sensitivity, one shortcoming of these materials in terms of future downsizing is the difficulty in dimension reduction, thus limiting the areal density of devices. Graphene (G) is a two-dimensional Dirac semimetal with a very high mobility of charge carriers.[2−5] The small spin orbit coupling combined with a high spin diffusion length makes graphene attractive for applications in magnetoelectronics and magnetic sensing. Large magnetoresistance values have been observed for graphene-based structures. For example, MR in the range 60−100% has been observed in epitaxial monolayer and multilayer graphene (300 K, 9 T) and layer-by-layer stacked few-layer graphene (300 K, 14 T).[6−8] Thus far, turbostratic multilayer graphene is the choice platform for making MR-based magnetic sensors, since its interlayer interactions significantly increase the MR effect.[9,10] In contrast to graphite, the 2D massless Dirac fermion is preserved in turbostratic multilayer graphene due to the decoupling of adjacent rotationally misaligned layers. In particular, the nonsaturating linear magnetoresistance of multilayer graphene is attractive for magnetic sensing applications. Different mechanisms have been suggested for the MR effects in multilayer graphene, ranging from the presence of high- and low-resistance channels in these multilayers, as well as interlayer tunnelling through the Landau levels of different graphene layers when a perpendicular magnetic field is applied.[9] Nevertheless, a number of practical problems need to be resolved before reliable multilayer graphene-based MR devices can be realized. Although turbostratic graphene can be directly grown on nickel by CVD, the films so-obtained are often nonuniform with respect to thickness, and a precise control of the layer number remains challenging. Batch-to-batch variation in crystalline quality and

Received: January 11, 2018
Revised: April 25, 2018
Published: May 4, 2018

Downloaded via NATL UNIV OF SINGAPORE on July 2, 2018 at 05:28:55 (UTC).
See https://pubs.acs.org/sharingguidelines for options on how to legitimately share published articles.

ACS Publications © 2018 American Chemical Society

DOI: 10.1021/acs.nanolett.8b00155
Nano Lett. 2018, 18, 3377−3383

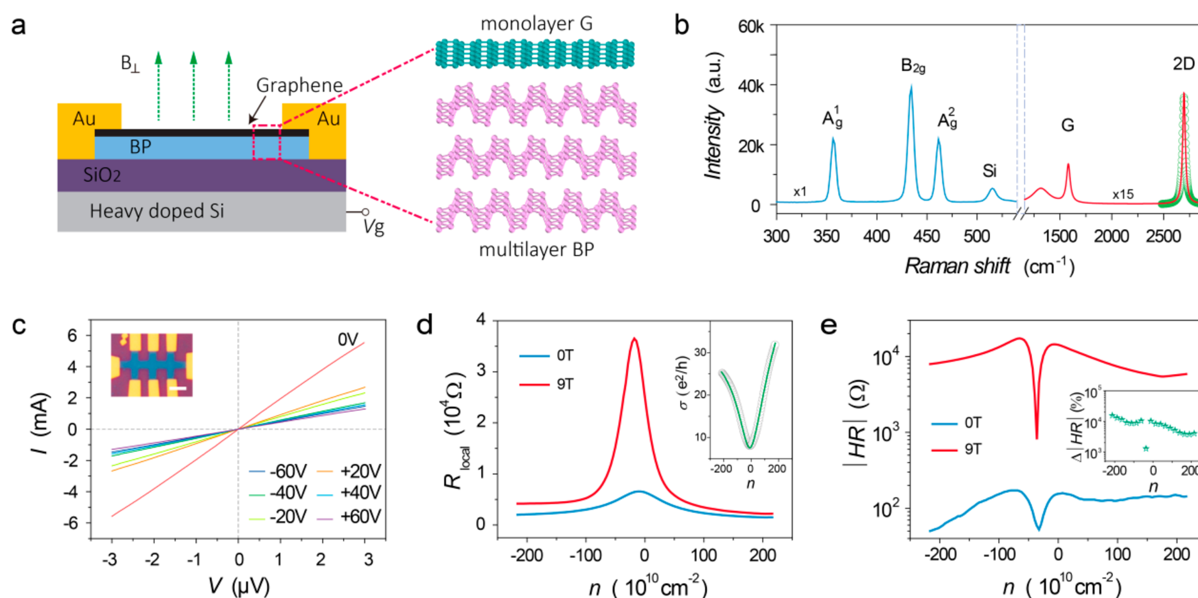

Figure 1. Schematic drawing and performance of monolayer graphene on multilayer BP flake (G/BP) device. (a) Schematic illustration of a gated G/BP device. The electrostatic gate voltage is applied to the G/BP sample through a p-doped silicon wafer, and the external magnetic field is applied perpendicular to the basal plane. (b) Raman spectrum of the G/BP heterostructure showing intrinsic features of BP in the low-wavenumber region and those of G at high wavenumbers. (c) $I-V$ curves of the gated G/BP device with Hall bar geometry. Linear curves show ohmic contact of the sample with metal electrodes. Scale bar for inserted optical image is 2 μm. (d, e) Longitudinal resistance and hall resistance (HR) at 300 K under varying electric field strength and magnetic fields. Inset in part d is the fitting of the effective medium theory conductivity of the G/BP device at zero magnetic field. Inset plot in part e is the increment of hall resistance (Δ|HR|) from 0 to 9 T at different carrier densities.

thickness of CVD-grown few-layer graphene may compromise reproducibility in MR devices.[10] In contrast, rapid progress has been achieved in growing large area, highly crystalline monolayer graphene, thereby raising the prospect of fabricating MR devices based on monolayer graphene. It is therefore timely to explore whether a giant MR effect comparable to that observed in multilayer graphene can be achieved in monolayer graphene. This is particularly motivated by the inherent sensitivity of graphene's electronic properties to disorder, interfacial strain, or phonon-mediated effects, through the tailoring of which giant MR effects may be obtained.

The origin of the observed MR in graphene has been attributed to stochastic spatial fluctuations in carrier mobility due to charge inhomogeneity or disorder; such disorder may come about from both inherent defects and extrinsic electron scattering sites, although a microscopic picture of this macroscopic effect is currently lacking. Previous works reported various methods to enhance the MR of single-layer graphene, for example, by decorating it with gold nanoparticles (MR ~ 480% at 300 K and 10 T), by fluorination, or by nitrogen doping (negative MR).[11−13] Common to all, the spatial inhomogeneities introduced by the dopants have the effect of interrupting the single electronic bands of graphene. However, due to the highly variable spatial distribution of the dopants or surface atoms, there is a high degree of uncertainty in achieving the desired control over carrier mobility.

Large MR has been reported from a graphene−hexagonal boron nitride (*h*-BN) heterostructure device.[14,15] In this architecture, a MR of ~880% for four-layer graphene (400 K and 9 T) and ~2000% for six-layer graphene (400 K and 9 T) near the Dirac point can be achieved. However, devices requiring precise number of graphene layers are very challenging to fabricate. It would be more convenient to use monolayer graphene to fabricate magnetic sensors in view of the fact that the production of large area monolayer graphene on copper foil has entered the first stage of commercialization.

Black phosphorus (BP), a layered allotrope of elemental phosphorus, has emerged as a promising 2D semiconductor.[16−18] At room temperature (300 K), due to the lower Debye temperature of BP (500 K for BP, in contrast to 2300 K for G), the phonon−phonon scattering rate of BP is much higher than that in SiO_2; the latter has only two surface optical phonon modes (59 and 155 meV),[19,20] whereas BP has nine low-energy optical phonon modes in the range 17−66 meV owing to its four P atoms per primitive unit cell. Besides, the phonon spectrum of BP has three acoustic branches: the *z*-direction acoustic (ZA) mode, the in-plane transverse acoustic (TA) mode, and the longitudinal acoustic (LA) mode, which makes BP a strongly phonon-active material at room temperature. A large linear MR of few-layer BP (~50% at 7 T and 300 K) was recently reported; the positive MR is found to increase by an order of magnitude when the temperature is decreased to 30 K (510% at 7 T). This large increase has been attributed to a classic MR effect originating from mobility fluctuation.[21]

In this work, we discover a phonon-mediated colossal MR effect on a vertical heterostructure consisting of monolayer graphene stacked on few-layer BP. Few-layer BP was chosen as a substrate to invoke a large MR response on monolayer graphene due to its finite direct band gap, high mobility, and anisotropic properties. Our analysis shows that the coupling of carriers in graphene to the polar optical phonons localized near the G/BP interface leads to mobility fluctuations and a large increase in MR across wide carrier densities. Most importantly, this work highlights how interface phonons can be harnessed to modulate a large MR response in graphene.

To fabricate a G/BP van der Waals heterostructure, a multilayer BP flake was first exfoliated onto a Si/SiO_2 substrate, followed by the transfer of a graphene monolayer on top of the

DOI: 10.1021/acs.nanolett.8b00155
Nano Lett. 2018, 18, 3377−3383

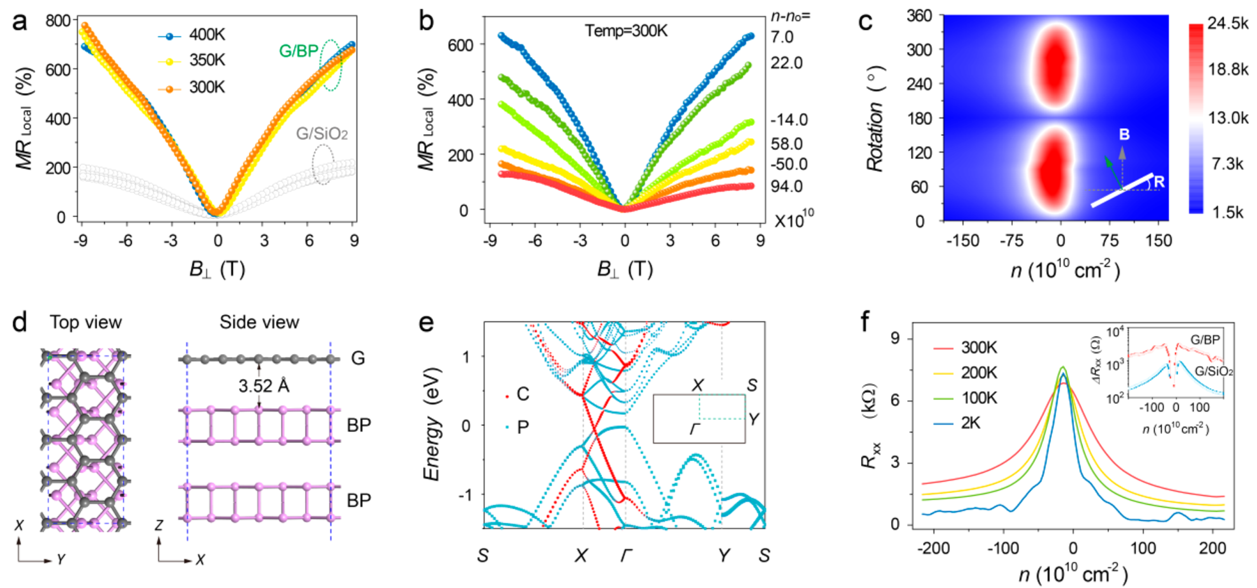

Figure 2. Giant magnetoresistance performance of G/BP heterostructure with a working temperature up to 400 K. (a) Magnetoresistance (MR) of G/BP and G/SiO_2 devices at various temperatures. The colored solid symbols represent data for G/BP while gray open symbols show MR of pristine G on SiO_2 (temperature: 300−400 K). (b) MR of a G/BP device at different carrier densities (300 K). (c) Two-dimensional map of the magnetic resistance of G/BP device exposed to 9 T field versus electrostatic gating and angle of rotation of the magnetic field with respect to the device plane (T = 300 K). (d, e) Lattice and electronic band structure of G/BP heterostructure. For the calculation, the graphene zigzag edge was aligned with the zigzag direction of BP. The zigzag and armchair direction of BP was marked with X and Y, respectively. (f) Dependence of the longitudinal resistance R_{xx} on carrier density at various temperatures. Inset plot shows the comparison of the temperature-dependent variation of R_{xx} for both the G/BP and G/SiO_2 devices. The variation of R_{xx} with temperature is given by the relation $\Delta R_{xx} = R_{xx}(300\ \text{K}) - R_{xx}(2\ \text{K})$.

BP in an argon-filled glovebox using standard dry-transfer procedures; more information on the experimental procedure is given in previous works.[22] Figure 1a sketches the cross section of our G/BP (G on few-layer BP) Hall bar device with multiple Au electrical contacts on top of the graphene film placed on a silicon wafer with a 300 nm oxide layer (the inset in Figure 1c shows the top-view of the G/BP device, Supporting Figure S1 for AFM image). To form good electrical contacts and minimize sample degradation, the device was thermally annealed in ultrahigh vacuum (10^{-10} Torr) to remove impurities (see the Methods section). The crystalline structures of graphene and BP were characterized using Raman spectroscopy. Figure 1b shows the Raman spectrum with three intrinsic low-frequency peaks at ~356.7, 433.9, and 461.8 cm^{-1}, which are attributed, respectively, to the A_g^1, B_{2g}, and A_g^2 phonon modes arising from the orthorhombic crystal structure of few-layer BP (for crystalline orientation and oxidation, see Figure S2). In the high-frequency region, the G peak (centered ~1581 cm^{-1}, corresponding to the high-frequency E_{2g} phonon at Γ point) and the 2D peak (centered ~2694 cm^{-1}, due to second-order Raman scattering by two optical phonons) of graphene are observed; the latter fits well to a single Lorentzian, which is a clear signature of single-layer graphene.[17,23] The MR of the heterostructure was measured at various temperatures in four-point geometry using standard low-frequency lock-in techniques. All measurements were conducted in vacuum (<1 × 10^{-6} mbar) to exclude the effect of adsorbates.

To probe the electrical conduction of graphene on BP, four-probe $I-V$ measurements were carried out. The $I-V$ profiles are plotted in Figure 1c. A linear $I-V$ behavior is seen at all gate voltages (V_g = 0 V, ± 20 V, ± 40 V, and ±60 V), indicating ohmic contacts at both hole and electron sides of the gate doping. Figure 1d shows the local longitudinal resistivity (R_{xx}) of the G/BP device as a function of the carrier density (n) at zero magnetic field at 300 K (blue curve). R_{xx} (blue line in Figure 1d) rises to ~1 kΩ at high carrier density and shows a sharp peak (close-up view in Figure S3) at $n_0 \approx -12 \times 10^{10}$ cm^{-2}, which is assigned to the charge-neutral Dirac point (CNP) of graphene. After suppressing thermal effects and phonon scatterings by cooling the G/BP device below 2 K, R_{xx} at high carrier density region reduces to ~100 Ω (see Figure 2f and Figure S4d).[24,25] The conduction contribution from the underlying BP flake to the overall MR is expected to be negligible due to its greater than 1 order of magnitude lower charge mobility with respect to graphene, as well as the asymmetric hole/electron mobility in few-layer BP.[3,16,18,24]

To investigate the MR effect in the G/BP system, a magnetic field of 9 T was applied perpendicular to the G/BP plane. MR is defined as MR = $[R_{xx}(B) - R_{xx}(0)]/R_{xx}(0)\cdot 100\%$, where $R_{xx}(B)$ and $R_{xx}(0)$ are the resistivity values at field B and at zero field, respectively. As shown in Figure 1d,e (red curves), a significant increase is observed for both the local longitudinal magnetoresistance and the Hall resistance (HR) across the entire range of carrier densities. The MR of the G/BP device increases to ~710% near the Dirac point, after which it gradually decreases with increasing carrier density (n) but remains >100% at $n \approx \pm 2 \times 10^{12}$ cm^{-2}. The increment in hall resistance (ΔHR) is >3500% in the whole measured range of carrier densities and even shoots up to >15 000% at $n < -205 \times 10^{10}$ cm^{-2}. It is known that, for a disordered 2D electron system, a positive MR is induced by inhomogeneity in carrier density (n_{rms}) and fluctuations in mobility ($\Delta\mu$).[5,14,15,26,27] To determine n_{rms} and $\Delta\mu$, the experimental data $\sigma(n - n_0)$ was fitted by effective medium theory (EMT); the fit is shown in the inset in Figure 1c.[26,28] The values of μ and n_{rms} extracted from the fits are used to calculate the Boltzmann-RPA (where RPA: random-phase approximation) conductivity resulting from screened Coulomb scattering. We also define a parameter

DOI: 10.1021/acs.nanolett.8b00155
Nano Lett. 2018, 18, 3377−3383

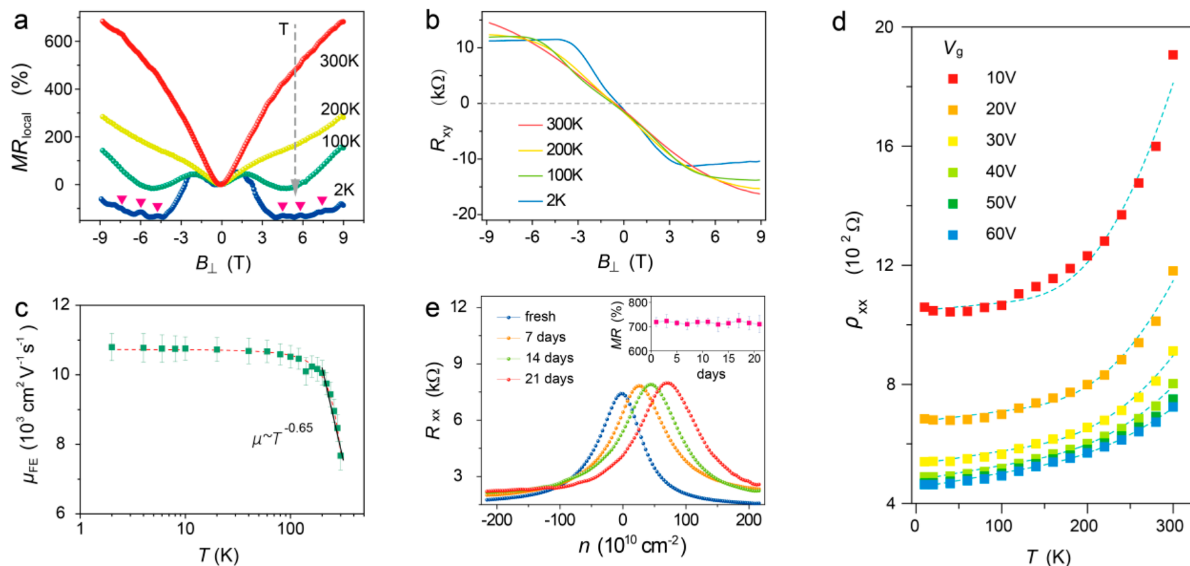

Figure 3. Temperature-dependent magnetoresistance performance and stability test of a G/BP sample. (a) Local MR versus magnetic field at various temperatures from 300 to 2 K. (b) Magnetic field dependence of the hall resistance R_{xy} at selected temperatures. (c) Temperature-dependent carrier mobility of monolayer graphene supported on a BP flake. (d) Resistance of G/BP samples as a function of temperature for gate voltages from 10 to 60 V. The solid symbols are experimentally observed values. Dashed blue lines are fits to eq 1 by considering acoustic phonon scattering in graphene and optical phonon scattering by the BP substrate. (e) Stability test of G/BP sample at room temperature; inset shows a plot of the MR against time for up to 21 days.

called short-range conductivity (σ_s) that is relevant at high carrier density where the conductivity saturates. σ_s is used to calculate the Boltzmann-RPA conductivity due to short-range scattering. The Boltzmann-RPA conductivity $\sigma_B[n_{rms}, \mu, \sigma_s]$ is related to the zero magnetic field EMT conductivity according to the equation $\int_{-\infty}^{\infty} dn\, A[n, n_0, n_{rms}] \frac{\sigma_B(n) - \sigma_{EMT}}{\sigma_B(n) + \sigma_{EMT}} = 0$, where $A[n, n_0, n_{rms}]$ is a Gaussian distribution centered at the average carrier density n_0, with a fluctuation of n_{rms}. By fitting the conductivity vs carrier density curve, the carrier mobility for G/BP is estimated to be ~(9500 ± 700) $cm^2\ V^{-1}\ s^{-1}$ at 300 K with fluctuation of carrier density n_{rms} = (47.89 ± 7.59) × 10^{10} cm^{-2} and σ_s = (46.61 ± 1.80) e^2/h (Figure S4c). As a control experiment, a monolayer graphene device with the same geometry and dimensions on SiO_2 substrate was fabricated. The values of carrier mobility, carrier density fluctuation, and short-range conductivity for the G/SiO_2 device are estimated to be ~12 900 ± 400 $cm^2\ V^{-1}\ s^{-1}$, 35.61 ± 2.84 × 10^{10} cm^{-2}, and 124.35 ± 4.61 e^2/h, respectively, at 300 K (Figure S4a); these values are comparable to those of the reported monolayer G/SiO_2 device.[15] By comparing the values between G/BP and G/SiO_2, we conclude that the G/BP device exhibits a larger fluctuation of carrier density and a lower carrier mobility.[29]

To distinguish the individual scattering contribution of impurities and phonons, we have measured the transport properties at different temperatures. At low temperatures (~1.5 K), the phonon modes of BP and G are suppressed significantly, and scattering by impurities dominates. For the G/BP device, the carrier mobility, fluctuation of carrier density n_{rms}, and short-range conductivity are determined to be ~ (13 100 ± 1200) $cm^2\ V^{-1}\ s^{-1}$, (26.00 ± 5.94) × 10^{10} cm^{-2}, and (71.47 ± 6.02) e^2/h (Figure S4d), respectively, at ~1.5 K. At 300 K, n_{rms} of the G/BP device increases to (47.89 ± 7.59) × 10^{10} cm^{-2}, which is higher than that of the control G/SiO_2 device (n_{rms} = 35.61 ± 2.84 × 10^{10} cm^{-2}); therefore this reflects that, at room temperature, the scattering from the BP substrate creates a much stronger charge inhomogeneity in graphene compared to SiO_2 substrate.

The variation in local MR as a function of the magnetic field, measured at selected temperatures, is shown in Figure 2a. Between 300 and 400 K, our G/BP device shows a quadratic positive MR at low fields (threshold field ~0.9 T), which converts to a linear nonsaturating positive MR at high fields, characteristic of a classic MR behavior.[5,6] The maximum MR of G/BP device reaches ~775% ± 25% at 9 T ($n = n_0$) at 300 K, and increases to more than 700% at 400 K, which is 3 times higher than the highest reported value for exfoliated monolayer graphene on SiO_2 (please refer to Figure S5 for more statistical data).[15] The MR-to-field strength is measured to be >86% T^{-1}, which qualifies our device as a high-sensitivity magnetic field sensor. That our measurement method is robust is judged from the fact that the MR measured for the control G/SiO_2 device in the temperature range 300−400 K is ~200%, which is consistent with previously reported values.[8,15] Figure 2b displays the MR at different carrier densities at 300 K. Away from the Dirac point, the MR gradually decreases with increasing carrier density but remains >100% at a carrier density of 9.4 × 10^{11} cm^{-2}. In line with classic magneto-transport behavior, no saturation is observed at high carrier concentrations. Additional evidence for the classical MR behavior in our G/BP device comes from the dependence of MR on the orientation of the magnetic field with respect to the G/BP plane (Figure 2c); R_{xx} reaches a maximum when the magnetic field is normal to the plane of the film (R = 90° and 270°) and has the minimum value when R = 0° and 180°.

To investigate if the large MR is due to interface states at the G/BP interface, we have performed a density functional theory (DFT) calculation to investigate electronic properties of G/BP heterostructure (see the SI for calculation details). The interlayer distance between graphene and bilayer BP is calculated to be 3.52 Å (Figure 2d); this van der Waals gap confirms the weak nature of the interfacial interaction, in good

DOI: 10.1021/acs.nanolett.8b00155
Nano Lett. 2018, 18, 3377−3383

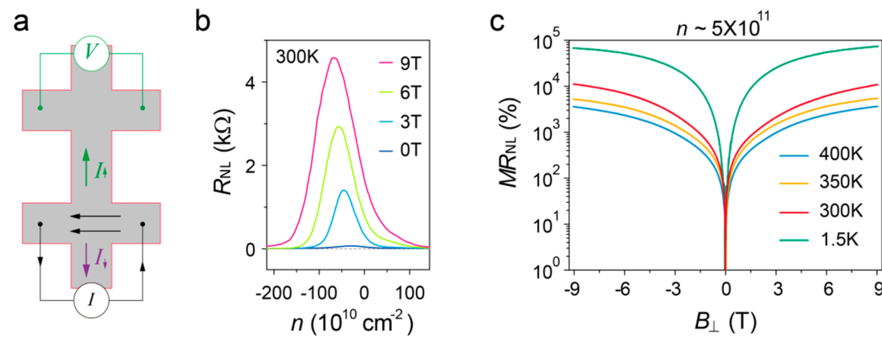

Figure 4. Nonlocal magnetoresistance performance of a G/BP device. (a) Sketch of the nonlocal geometry showing a transverse spin current in the presence of a Lorentz force. (b) Nonlocal response from a G/BP device at 300 K. The slight shifting of the Dirac point as a function of the magnetic field is attributed to temperature-induced resistance fluctuations arising from both Nernst and Ettingshausen effects.[41] (c) Nonlocal MR from a G/BP device at various temperatures near the Dirac point.

agreement with previous studies.[30] Figure 2e shows the electronic band structure of the G/BP heterostructure, and it is clear that both the projected band structures of graphene and BP maintain the characteristics of their isolated counterparts; thus we can conclude that the origin of large MR in the G/BP heterostructure is not due to interface state.

The temperature dependence of resistivity offers insights into the mechanism of the phonon-mediated MR observed in the G/BP device. As shown in Figure 2f, the resistivity changes from nonmetallic to a metallic behavior when the carrier density increases from the Dirac point (see Figure S6 for temperature-dependent resistance of the G/SiO_2 device). However, a major difference is that there is a very large increase in resistivity [$\Delta R_{xx} = R_{xx}(300\text{ K}) - R_{xx}(2\text{ K})$] with decreasing T for the G/BP device. The observed ΔR_{xx} of the G/BP device is nearly 1 order of magnitude higher than that measured for the G/SiO_2 device. In the case of the G/BP device, a large ΔR_{xx} showing a strong temperature dependence persists both near the Dirac point, as well as far away from it, suggesting that both long-range and short-range phonon scattering is operational.[31]

The MR of the G/BP device as a function of B and T ($n = n_0$) is presented in Figure 3a. The MR decreases with temperature for the G/BP device, and once the temperature is below 100 K, a negative MR originating from weak localization appears. At 2 K, symmetric oscillation patterns are seen at positive and negative magnetic fields, indicating the presence of universal conductance fluctuation (UCF) resulting from multiple scattering of a coherent electron wave while traversing a disordered conductor.[32] The observation of weak localization (WL) and UCF effects suggests that G/BP is a highly disordered 2D electronic system.[32−34] It should be pointed out here that, for MR devices fabricated using monolayer G on SiO_2, the MR effect is mainly attributed to mobility and its fluctuations, in which case the carrier mobility increases with decreasing temperature, and a higher MR is expected at lower temperatures.[35] In contrast, MR increases dramatically with temperature for our G/BP device due to phonon scattering by the underlying BP, which creates many low-mobility islands in the graphene lattice. Under an electric field, an effective drift velocity is generated in a direction perpendicular to the cycloid motion of the charge carriers caused by multiple small-angle scattering near low-mobility islands, which results in a linear MR due to the deflection of cycloid motion by the low-mobility islands.[36] At lower temperatures, phonon scattering is suppressed, and this reduces the population of low-mobility islands, thereby lowering the linear MR response. Figure 3b shows the dependence of Hall resistance (R_{xy}) on the applied magnetic field at selected temperatures. At 300 K, R_{xy} is almost linearly proportional to the magnetic field; the negative slope indicates that the majority carriers are electrons (one-band behavior). At ~2 K, because of the robust localization effect of electrons, R_{xy} shows quantum behavior and saturates above 3 T.

Similar to other 2D electron gas systems such as $Al_xGa_{1-x}As$/GaAs, the carrier mobility of graphene is limited by phonon scattering at high temperatures.[20,37] At $T < 100$ K, the field effect carrier mobility saturates at ~10 500 ± 304 cm^2 V^{-1} s^{-1} (Figure 3c), which means that disorder-induced scattering dominates over phonon scattering in this temperature range and limits the carrier mobility. At higher temperatures ($T > 100$ K), phonon scattering dominates, and the carrier mobility decreases with the increasing T following a nonlinear dependence in the form $\mu \propto T^{-\gamma}$ ($\gamma \approx 0.65 \pm 0.12$). A small γ value implies that scattering by the optical phonon predominates over that of the acoustic phonon at these temperatures.[24] Next, we have separated the contribution due to phonon scattering by investigating the change in resistivity while tuning the carrier density by varying the gate voltage (Figure 3d). The resistivity $\rho(T, n)$ curves are linear with respect to temperature at low T and become highly nonlinear at higher T. Moreover, the resistivity is strongly dependent on the carrier density (n) and increases for decreasing n. Summing over the possible contributions from all phonons, we can write

$$\rho(T, n) = \rho_0(0, n) + \rho_{LA}(T) + \rho_B(T, n) \quad (1)$$

where ρ_0, ρ_{LA}, and ρ_B represent scattering by impurities (the residual resistivity at low temperature), LA phonons ($\rho_{LA}(T) = [(h/e^2)\pi^2 D_A^2 k_B/(2h^2\rho_s v_s^2 v_F^2)]\cdot T$), and optical phonon [$\rho_B(T, n) \sim (e^{E_0/k_BT} - 1)^{-1}$], respectively.[20,38] Longitudinal acoustic (LA) phonon scattering in graphene is linearly proportional to T and will give rise to a linear resistivity, which is independent of carrier density. Therefore, it is clear that the nonlinear behavior at higher T can be attributed to optical phonon scattering $\rho_B(T, n)$. Using the optical phonon scattering model, the temperature-dependent resistivity at different carrier densities fit well to eq 1. We now discuss the different possible origins of optical phonon scattering. In graphene, besides the LA phonon, two other modes exist: the zone boundary ZA phonon (~70 meV) and the optical ZO mode (~110 meV). However, both these modes are out-of-plane vibrations and have been observed to not couple strongly to electrons.[39] Apart from these modes, the

DOI: 10.1021/acs.nanolett.8b00155
Nano Lett. 2018, 18, 3377−3383

most likely source of optical phonon scattering observed in our sample is from the BP substrate, which contains a number of active phonon modes. These phonons are expected to influence the transport of graphene in two ways. First, the phonons from BP can break the inversion symmetry of graphene and induce an additional perturbation potential in graphene. Second, BP phonons may evoke a long-range potential and lead to a carrier-density-dependent resistance of graphene by electron−phonon scattering, in a similar manner to scattering by charged impurities.[40] The exact mechanism for this phonon-mediated MR is not understood at present and requires further studies.

Finally, the encapsulation of BP by the graphene sheet improves the stability of the G/BP MR device significantly. After exposure to air (humidity ∼70−80% and $T \sim 25$−28 °C) for 21 days, the G/BP device shows a R_{xx} vs n curve that is mostly unchanged with respect to the initial device (Figure 3e) and maintains a steady MR of ∼720 ± 35%. A slight p-doping was present, which may be due to adsorbents or moisture; this was removed after thermal annealing. The air stability of the G/BP MR device demonstrates that it can be used to build stable magnetic sensors.

Nonlocal measurements performed in Hall bar geometry, where the voltage probes are remotely located from the classical path of charge flow (as sketched in Figure 4a), are sensitive to magneto-transport phenomena near the Dirac point. In the presence of a magnetic field, Zeeman splitting lifts the spin/valley degeneracy in graphene resulting in a large nonlocal magnetoresistance near the Dirac point of graphene at room temperature.[41] The nonlocal magnetoresistance of graphene may be further enhanced via spin−orbit interaction or spin−orbit proximity effect when graphene is stacked on a spintronic material.[42] Since BP is reported to be a promising spin channel material with a spin relaxation length >6 μm at room temperature,[43] using BP as the substrate can potentially increase the nonlocal MR value in G. To minimize contributions from inductive coupling and thermal effects, both dc and low-frequency ac measurements were carried out with a drive current of 100 nA. In this geometry, the ohmic contribution to the measured nonlocal signal is very small and decreases exponentially with L according to the relation $R_{NL} \approx (4/\pi)\rho_{xx} \exp(-\pi L/W)$ where L is the separation between current and voltage probes, and W is the channel width. As shown in Figure 4b, the nonlocal R_{NL} vs carrier density curve (300 K) exhibits a resistance peak at the Dirac point with a magnitude that is dependent on the magnetic field. The observed nonlocal MR is qualitatively similar to that reported for G on h-BN and SiO_2 substrates, which have been explained by the spin/valley Hall effect.[41] Remarkably, the G/BP device (channel dimension: $L \times W = 5\ \mu m \times 1\ \mu m$) exhibits a high R_{NL} value of ∼4.4 kΩ at 9 T (>11 000 Ω at 9 T, ∼1.5 K, Figure S10) near the vicinity of the Dirac point, which is the highest observed value for a graphene-based nonlocal device to date. Consequently, the MR measured in nonlocal geometry is ∼10 000% even at room temperature (Figure 4c), which is 4 times higher than that for the G/h-BN device (∼2300−2600% at 9 T, 300 K) and 100 times larger than that observed for G/SiO_2 (∼80−120% at 9 T, 300 K).[41] The nonlocal MR further reaches ∼70 000% at 9 T and <2 K, which provides further proof that the huge nonlocal response of the G/BP device arises from a temperature-dependent spin/valley Hall effect rather than being thermally induced.[44]

In conclusion, we have observed colossal MR from a vertical heterostructure constructed by stacking monolayer G on BP, with a local MR reaching ∼775% at 9 T and 300 K. The average MR values of our 2D G/BP heterostructure are several times larger than those of the conventional magnetic tunnelling junction (∼220% at room temperature)[45,46] as well as emerging organic spin-valves (∼40%);[47] it is also comparable to the state-of-the-art MgO tunnel barrier (∼500%)[48] and pseudo-spin-valve magnetic tunnel junction (604% at 300 K).[49] In the nonlocal geometry, the measured MR is ∼10 000% near the Dirac point. Importantly, our results suggest that colossal MR can be achieved in the heterostructure due to the sensitivity of monolayer graphene to the strong surface polaronic effects on BP; the latter influences the high-temperature mobility and hot-electron properties of graphene stacked on it. The phonon-mediated MR observed here for our monolayer-on-BP device is distinct from previous MR devices made from multilayer G, which rely on interlayer effects between randomly stacked graphene layers. As opposed to the impurity model where a larger MR response is obtained at lower temperatures, the phonon-mediated MR has its largest value at near ambient temperatures of 300−400 K. This useful operating temperature range combined with the improved stability of the graphene-encapsulated G/BP device structure presents enticing prospects for making a highly sensitive MR device.

Methods. *Device Fabrication.* The exfoliation of BP was carried out in a glovebox filled with argon (O_2 and H_2O levels <0.5 ppm). Typically, a thin BP flake was directly mechanically exfoliated from a bulk BP crystal (HQ graphene) onto a silicon substrate using blue "magic" tape. Using optical microscopy under argon atmosphere to avoid degradation of BP, the desired BP flake was identified. Monolayer graphene was exfoliated from Kish graphite and aligned onto the BP flake with desired rotation angle with the assistance of a transfer platform. This transfer process was also carried out inside the Ar-filled glovebox.[22,50,51]

Device Characterization. The thickness and morphology of the devices were verified using a Dimension FastScan AFM (Bruker) instrument in tapping mode. The orientations of the BP flake with respect to graphene were determined from angle-resolved polarized Raman (Renishaw) spectra and polarized optical microscopy (Nikon).

Electrical Transport Measurements. The measurements were carried out in both a ^{4}He cryostat (TeslatronPT) and a physical property measurement system (PPMS) under helium atmosphere using standard alternating-current (ac) lock-in amplifiers (SR830) and direct-current (dc) techniques. Resistance vs temperature and field measurements were performed using low currents in the range 50−300 nA to avoid Joule heating. To avoid mixing of the longitudinal and transverse components due to sample geometry, we have performed standard symmetrizing and antisymmetrizing procedures to obtain pure R_{xx} and R_{xy}, as both positive and negative field curves have been measured.

■ ASSOCIATED CONTENT

Supporting Information

The Supporting Information is available free of charge on the ACS Publications website at DOI: 10.1021/acs.nanolett.8b00155.

Details of AFM image, Raman spectrum, EMT conductivity of the G/BP and G/SiO_2 device, band structure calculations, proposed mechanism, low-T nonlocal response, and additional MR data (PDF)

DOI: 10.1021/acs.nanolett.8b00155
Nano Lett. 2018, 18, 3377−3383

AUTHOR INFORMATION

Corresponding Author

*E-mail: chmlohkp@nus.edu.sg. Phone: +65 6516 2658. Fax: +65 6779 1691.

ORCID

Yanpeng Liu: 0000-0002-5265-2735
Yong Zheng Luo: 0000-0002-5142-2508
Jianyi Chen: 0000-0002-3757-7634
Kian Ping Loh: 0000-0002-1491-743X

Notes

The authors declare no competing financial interest.

ACKNOWLEDGMENTS

We are grateful for financial support from National Research Foundation, Prime Minister's Office, Singapore, Grant NRF-NRFI2015-01 "Graphene Oxide-A New Class of Catalytic, Ionic and Molecular Sieving Materials".

REFERENCES

(1) Baibich, M. N.; Broto, J. M.; Fert, A.; Van Dau, F. N.; Petroff, F.; et al. *Phys. Rev. Lett.* **1988**, *61*, 2472−2475.
(2) Moodera, J. S.; Kinder, L. R.; Wong, T. M.; Meservey, R. *Phys. Rev. Lett.* **1995**, *74*, 3273−3276.
(3) Novoselov, K. S.; Geim, A. K.; Morozov, S. V.; Jiang, D.; Zhang, Y.; Dubonos, S. V.; Grigorieva, I. V.; Firsov, A. A. *Science* **2004**, *306*, 666−669.
(4) Castro Neto, A. H.; Guinea, F.; Peres, N. M. R.; Novoselov, K. S.; Geim, A. K. *Rev. Mod. Phys.* **2009**, *81*, 109−162.
(5) Sarma, S. D.; Adam, S.; Hwang, E. H.; Rossi, E. *Rev. Mod. Phys.* **2011**, *83*, 407.
(6) Wang, W. J.; Gao, K. H.; Li, Z. Q.; Lin, T.; Li, J.; Yu, C.; Feng, Z. H. *Appl. Phys. Lett.* **2014**, *105*, 182102.
(7) Friedman, A. L.; Tedesco, J. L.; Campbell, P. M.; Culbertson, J. C.; Aifer, E.; Perkins, F. K.; Myers-Ward, R. L.; Hite, J. K.; Eddy, C. R., Jr; Jernigan, G. G.; Gaskill, D. K. *Nano Lett.* **2010**, *10*, 3962−3965.
(8) Chen, J. J.; Meng, J.; Zhou, Y. B.; Wu, H. C.; Bie, Y. Q.; Liao, Z. M.; Yu, D. P. *Nat. Commun.* **2013**, *4*, 1921.
(9) Bodepudi, S. C.; Wang, X.; Pramanik, S. *J. Appl. Phys.* **2015**, *118*, 164303.
(10) Bodepudi, S. C.; Singh, A. P.; Pramanik, S. *Nano Lett.* **2014**, *14*, 2233−2241.
(11) Jia, Z.; Zhang, R.; Han, Q.; Yan, Q.; Zhu, R.; Yu, D.; Wu, X. *Appl. Phys. Lett.* **2014**, *105*, 143103.
(12) Hong, X.; Cheng, S. H.; Herding, C.; Zhu, J. *Phys. Rev. B: Condens. Matter Mater. Phys.* **2011**, *83*, 085410.
(13) Rein, M.; Richter, N.; Parvez, K.; Feng, X.; Sachdev, H.; Kläui, M.; Müllen, K. *ACS Nano* **2015**, *9*, 1360−1366.
(14) Gopinadhan, K.; Shin, Y. J.; Jalil, R.; Venkatesan, T.; Geim, A. K.; Neto, A. H. C.; Yang, H. *Nat. Commun.* **2015**, *6*, 8337.
(15) Gopinadhan, K.; Shin, Y. J.; Yudhistira, I.; Niu, J.; Yang, H. *Phys. Rev. B: Condens. Matter Mater. Phys.* **2013**, *88*, 195429.
(16) Li, L.; Yu, Y.; Ye, G. J.; Ge, Q.; Ou, X.; Wu, H.; Feng, D.; Chen, X. H.; Zhang, Y. *Nat. Nanotechnol.* **2014**, *9*, 372−377.
(17) Ling, X.; Wang, H.; Huang, S.; Xia, F.; Dresselhaus, M. S. *Proc. Natl. Acad. Sci. U. S. A.* **2015**, *112*, 4523−4530.
(18) Liu, Y. P.; Qiu, Z. Z.; Carvalho, A.; Bao, Y.; Xu, H.; Tan, S. J. R.; Liu, W.; Castro Neto, A. H.; Loh, K. P.; Lu, J. *Nano Lett.* **2017**, *17*, 1970−1977.
(19) Jain, A.; McGaughey, A. J. *Sci. Rep.* **2015**, *5*, 8501.
(20) Chen, J. H.; Jang, C.; Xiao, S.; Ishigami, M.; Fuhrer, M. S. *Nat. Nanotechnol.* **2008**, *3*, 206−209.
(21) Hou, Z.; Yang, B.; Wang, Y.; Ding, B.; Zhang, X.; Yao, Y.; Liu, E.; Xi, X.; Wu, G.; Zeng, Z.; Liu, Z. *Sci. Rep.* **2016**, *6*, 23807.
(22) Geim, A. K.; Grigorieva, I. V. Van der Waals heterostructures. *Nature* **2013**, *499*, 419−425.
(23) Liu, Y.; Yuan, L.; Yang, M.; Zheng, Y.; Li, L.; Gao, L.; Nerngchamnong, N.; Nai, C. T.; Sangeeth, C. S.; Feng, Y. P.; Nijhuis, C. A.; Loh, K. P. *Nat. Commun.* **2014**, *5*, 5461.
(24) Long, G.; Maryenko, D.; Shen, J.; Xu, S.; Hou, J.; Wu, Z.; Wong, W. K.; Han, T.; Lin, J.; Cai, Y.; Lortz, R. *Nano Lett.* **2016**, *16*, 7768−7773.
(25) Deng, B.; Tran, V.; Xie, Y.; Jiang, H.; Li, C.; Guo, Q.; Wang, X.; Tian, H.; Koester, S. J.; Wang, H.; Cha, J. J. *Nat. Commun.* **2017**, *8*, 14474.
(26) Adam, S.; Hwang, E. H.; Galitski, V. M.; Sarma, S. D. *Proc. Natl. Acad. Sci. U. S. A.* **2007**, *104*, 18392−18397.
(27) Tiwari, R. P.; Stroud, D. *Phys. Rev. B: Condens. Matter Mater. Phys.* **2009**, *79*, 165408.
(28) Ping, J.; Yudhistira, I.; Ramakrishnan, N.; Cho, S.; Adam, S.; Fuhrer, M. S. *Phys. Rev. Lett.* **2014**, *113*, 047206.
(29) Avouris, P.; Heinz, T. F.; Low, T. *2D Materials: Properties and Devices*; Cambridge University Press, 2017.
(30) Padilha, J. E.; Fazzio, A.; da Silva, A. J. R. *Phys. Rev. Lett.* **2015**, *114* (6), 066803.
(31) Min, H.; Hwang, E. H.; Sarma, S. D. *Phys. Rev. B: Condens. Matter Mater. Phys.* **2012**, *86*, 085307.
(32) Kharitonov, M. Y.; Efetov, K. B. *Phys. Rev. B: Condens. Matter Mater. Phys.* **2008**, *78*, 033404.
(33) McCann, E.; Kechedzhi, K.; Fal'ko, V. I.; Suzuura, H.; Ando, T.; Altshuler, B. L. *Phys. Rev. Lett.* **2006**, *97*, 146805.
(34) Chen, Y. F.; Bae, M. H.; Chialvo, C.; Dirks, T.; Bezryadin, A.; Mason, N. *J. Phys.: Condens. Matter* **2010**, *22*, 205301.
(35) Jabakhanji, B.; Kazazis, D.; Desrat, W.; Michon, A.; Portail, M.; Jouault, B. *Phys. Rev. B: Condens. Matter Mater. Phys.* **2014**, *90*, 035423.
(36) Kozlova, N. V.; Mori, N.; Makarovsky, O.; Eaves, L.; Zhuang, Q. D.; Krier, A.; Patanè, A. *Nat. Commun.* **2012**, *3*, 1097.
(37) Kawamura, T.; Sarma, S. D. *Phys. Rev. B: Condens. Matter Mater. Phys.* **1992**, *45*, 3612.
(38) Zou, K.; Hong, X.; Keefer, D.; Zhu, J. *Phys. Rev. Lett.* **2010**, *105*, 126601.
(39) Perebeinos, V.; Tersoff, J.; Avouris, P. *Phys. Rev. Lett.* **2005**, *94*, 086802.
(40) Fratini, S.; Guinea, F. *Phys. Rev. B: Condens. Matter Mater. Phys.* **2008**, *77*, 195415.
(41) Abanin, D. A.; Morozov, S. V.; Ponomarenko, L. A.; Gorbachev, R. V.; Mayorov, A. S.; Katsnelson, M. I.; Watanabe, K.; Taniguchi, T.; Novoselov, K. S.; Levitov, L. S.; Geim, A. K. *Science* **2011**, *332*, 328−330.
(42) Avsar, A.; Tan, J. Y.; Balakrishnan, J.; Koon, G. K. W.; Lahiri, J.; Carvalho, A.; Rodin, A.; Taychatanapat, T.; OFarrell, E.; Eda, G.; Neto, A. H. C. *Nat. Commun.* **2014**, *5*, 4875.
(43) Avsar, A.; Tan, J. Y.; Kurpas, M.; Gmitra, M.; Watanabe, K.; Taniguchi, T.; Fabian, J.; Özyilmaz, B. *Nat. Phys.* **2017**, *13*, 888−893.
(44) Renard, J.; Studer, M.; Folk, J. A. *Phys. Rev. Lett.* **2014**, *112*, 116601.
(45) Yuasa, S.; Nagahama, T.; Fukushima, A.; Suzuki, Y.; Ando, K. *Nat. Mater.* **2004**, *3*, 868−871.
(46) Parkin, S. S. P.; Kaiser, C.; Panchula, A.; Rice, P. M.; Hughes, B.; Samant, M.; Yang, S.-H. *Nat. Mater.* **2004**, *3*, 862−867.
(47) Xiong, Z. H.; Wu, D.; Vardeny, Z. V.; Shi, J. *Nature* **2004**, *427*, 821−824.
(48) Lee, Y. M.; Hayakawa, J.; Ikeda, S.; Matsukura, F.; Ohno, H. *Appl. Phys. Lett.* **2007**, *90* (21), 212507.
(49) Ikeda, S.; Hayakawa, J.; Ashizawa, Y.; Lee, Y. M.; Miura, K.; Hasegawa, H.; Tsunoda, M.; Matsukura, F.; Ohno, H. *Appl. Phys. Lett.* **2008**, *93* (8), 082508.
(50) Huang, Y.; Qiao, J.; He, K.; Bliznakov, S.; Sutter, E.; Chen, X.; Luo, D.; Meng, F.; Su, D.; Decker, J.; Ji, W.; Ruoff, R. S.; Sutter, P. *Chem. Mater.* **2016**, *28*, 8330.
(51) Doganov, R. A.; O'Farrell, E. C. T.; Koenig, S. P.; Yeo, Y.; Ziletti, A.; Carvalho, A.; Campbell, D. K.; Coker, D. F.; Watanabe, K.; Taniguchi, T.; Neto, A. H. C.; Özyilmaz, B. *Nat. Commun.* **2015**, *6*, 6647.

DOI: 10.1021/acs.nanolett.8b00155
Nano Lett. 2018, 18, 3377−3383